Journal of Applied Fluid Mechanics, Vol. 17, No. 12, pp. 2745-2760, 2024.
Available online at www.jafmonline.net, ISSN 1735-3572, EISSN 1735-3645.
https://doi.org/10.47176/jafm.17.12.2562

Numerical Study of the Three-Dimensional Laminar Flow around a Cubic Metal Foam Cell

A. Amroune† and B. Madani

Laboratory of Multiphase Transport and Porous Media (LTPMP), Faculty of Mechanical and Process Engineering (FGMGP)/ University of Sciences and Technology Houari Boumediene (USTHB), BP. 32, El Alia, 16111, Algiers, Algeria

Corresponding Author Email: aamroune@usthb.dz

ABSTRACT

The present study examines numerically a three-dimensional (3D) laminar and stationary flow around an idealized metal foam cell shaped as an empty cube with cylindrical edges. The physical configuration adopted consists of an isolated cell placed inside a plane channel crossed by air as a working fluid. The numerical investigation is carried out using the dimensionless Navier-Stokes equations resolved by finite volume method. The flow configurations given for several Reynolds numbers are described entirely using 2D and 3D maps. The plane maps give streamlines at the side and top fiber planes: the vertical side of the cell is normal to the flow. In addition, the critical locations and zones characterizing the flow are also localized: the saddle points, separation nodes, attachment points, foci of the recirculation zones, and the attachment lines. For the Reynolds number in the range $75 \leq \mathrm{Re} \leq 500$, the results show that the topography of the streamlines at the vertical plane in the middle of the lateral fibers of the cell ($z = 5{,}3D_P$) is developed into arc-shaped vortex rollers in the gap. In the wake, two saddle points reveal the zones of influence of these spiral structures, formed by two vortices (Bt and Nw) and zones of upwash and downwash. At a high value of Re ($Re = 500$), the upwash weakens but does not disappear. Two recirculation bubbles are associated with the two saddles, in the gap and the wake of the upper fibers, parallel to the flow. At Re =500, the distribution flow loses its symmetry and displays matter transfer between the two recirculation. The displacement of the saddle point in the wake is 9.65 times that in the gap. No vortex shedding is observed in the wake of cell due to the nullity of the frequency shedding ($f = 0$).The results indicate also that decreasing the pore diameter favors recirculation inside the cell gap. These recirculation lengths (L_{rz},L_{ry}) located respectively in the wake of planes $z = 5{,}3D_P$ and $y = D_P$ reduce the drag coefficient in equal proportion (51%) in the range $75 \leq Re \leq 500$. It appears that the wake of the lateral fibers of the z=5.3D_p plane contributes better to the drag coefficient. We consider that the predominance of downwash associated with the instability of saddle point S.2 in the wake when Re increases leads to a decrease in the drag coefficient in the wake.

Article History

Received February 10, 2024
Revised June 11, 2024
Accepted June 23, 2024
Available online October 2, 2024

Keywords:

Cell foam
Steamlines
Laminar flow
Vortices
Pressure coefficient

1. INTRODUCTION

A great number of Works on flow and heat transfer in metallic foam has been carried in the three past decades. Almost studies has been carried out experimentally and numerically using macroscopic approaches. In Madani et al. (2007) one could find an extensive literature study on the experimental works in the field. Numerically, the Representative Volume Elementary method (RVE) has been used largely. In the literature numerical studies on flow and heat transfer in metallic foam in the microscopic level are rare Ferfera & Madani (2020). Note that multi-functional exchangers for hydrogen production intensification are among industrial fields where metallic foam appliance is promising. This is showed by the results obtained by Abaidi and Madani (2020) using RVE method in studying reactive flow in vaporeformer. Based on data using by authors cited above, the aim of this study is to

Nomenclature

C_D	drag coefficient	u,v,w	velocity components
C_p	pressure coefficient	u_0	inlet velocity
D_f	fiber diameter	U,V,W	dimensionless components of velocity
D_P	pore diameter	x,y,z	system coordinates
G	cell form factor	X,Y,Z	dimensionless system coordinates
L_{ry}	recirculation length in plane $y = D_P$	**Greek symbols**	
L_{rz}	recirculation length in plane $z = 5.3D_P$	Δ	variation
p	pressure	ε	porosity of metal foam cell
Re	Reynolds number, $Re = \frac{\rho u_0 D_P}{\mu}$	μ	dynamic viscosity
S	Saddle point	ρ	fluid density

explore the flow behavior inside metallic foam at the microscopic level using Representative Cell Unit (RCU).

This work is part of the studies on the flow around obstacles. In this context, we examine the structure of the flow over a metal foam cell. Metal foams are three-dimensional cellular structures with a porosity exceeding 70%. In this sense, experimental and numerical studies have been carried out by many researchers. Saha (2004) completed a numerical study of three-dimensional laminar flow around a cubic configuration for $20 \le Re \le 300$. He concludes that the drag coefficient decreases and that the recirculation length increases as the Reynolds number increases. Backer (1979) experimentally demonstrated that horseshoe vortices are developed as the Reynolds number increases and the vortex system becomes complex and unstable. Abu-Qudais et al. (2001) analyzed two-dimensional laminar flow through a parabolic body. The obtained results show that pressure and skin friction increase with increasing Reynolds numbers. Visbal (1991) carried out a three-dimensional numerical study of the flow in the laminar regime through a cylindrical obstacle placed on a horizontal plate. The objective of this work is to study the formation of horseshoe vortices in stationary and periodic cases. He demonstrates that the saddle point which is formed in the front of the obstacle could be a point of attachment to the flow. Hwang and Yang (2004) examined numerically the vortex structures around a cubic obstacle placed in a parallelepiped channel at a moderate Reynolds number. They indicate that when the flow approaches the cube, an adverse pressure gradient occurs, generating a three-dimensional separation of the boundary layer and thus allowing the formation of horseshoe vortices. They add that when the Reynolds number increases further, the vortex system becomes more complicated, and the vortices increase in pairs. Liakos & Malamataris (2014) studied the three-dimensional stationary laminar flow around a cube placed in a parallelepiped channel. The results indicate the appearance of a tornado-like vortex next to the cube for all Reynolds numbers. Upstream of the obstacle, a horseshoe vortex is formed at Re = 1266. Launay et al. (2019) examine experimentally the interaction of emerging parallelepiped obstacle with free surface laminar flow. This generates three flow structures: a horseshoe vortex in front of the obstacle, two recirculation zones on the side surfaces, and a wake downstream. They prove by means of image velocimetry measurements (PIV) that the elongation of the obstacle, measured by the ratio (length/width), induces an adverse pressure gradient that relaxes the horseshoe vortex in the longitudinal directions. Klotz et al. (2014) used laser-induced fluorescence visualization (LIF) and particle image velocimetry (PIV) to experimentally examine the 3D flow structure in the wake behind a cube placed in a channel for Re varying from 100 to 400. The results reveal the existence of three regimes: an axisymmetric flow regime, another with two counter-rotating vortices, and a hairpin vortex detachment. The wake consists of four pairs of counter-rotating vortices with orthogonal symmetry. Behera and Saha (2019) use the D.N.S. (direct numerical simulation) method to study the characteristics of the 3D flow through a square cylinder at Re = 250. The authors show that the flow field behind the obstacle indicates the presence of two symmetrical and asymmetrical detachments for six boundary layer thicknesses $\left(\frac{\delta}{d}\right)$ varying from 0 to 0.30, contrary to perception, which suggests that the coexistence of these two modes of detachment does not occur only at a high Reynolds number. They added that increasing the thickness of the boundary layer could eventually produce a symmetrical detachment in the wake of the flow. Islam et al. (2014) investigated a numerical simulation of a 2D flow through a square cylinder upstream and a flat plate located downstream for Re between 75 and 200. The results obtained using the Boltzmann method (LBM) indicate that the development of the wake and vortex behind the cylinder depends considerably on the spacing ratio between the cylinder and plate and the Reynolds number (Re). They also showed that the root-mean-square of the drag and lift coefficients, for all spacing values, increases as the Reynolds number increases. Ma et al. (2019) used a physical model similar to that used by Islam et al. (2014). They proved that the rapprochement between the two obstacles eliminates the vortex detachment and reduces the drag force. Kumar & Singh (2019) studied numerically 2D flow characteristics in the wake of a cylinder function of the blockage ratio (BR) and Reynolds number (Re). The study is based on the volume method using the Ansys Fluent simulation code. They conclude that at a fixed

Reynolds number, the drag coefficient increases when the blockage ratio increases, and at a fixed blockage ratio, it decreases when the Reynolds number increases. Jiang & Cheng (2020) examined the flow separation around a parallelepiped body for Reynolds numbers between 40 and 400 using the direct numerical simulation method (D.N.S.). According to the study, the established models show that the separation of the flow does not occur at the sharp corners of the obstacle, for both time-averaged and instantaneous, for a range of moderate Reynolds numbers (10–400). However, it emerges downstream of the leading edge at a distance equivalent to a quarter of the length of the parallelepiped when the Reynolds number reaches the critical values of 100.36 and 96. They found that the three-dimensionality of the flow, which is developed at Re > 165.7, affects the location of the saddle point, but has almost no influence on the location of the separation point. Chen et al. (2022) numerically studied the 3D flow over two stationary side-by-side circular cylinders in the case with Re = 500 and a spacing ratio (s/D) varying from 1 to 5. The study revealed the existence of five flow regimes that essentially depend on spacing ratio: single bluff body flow at s/D =1.1, deflected flow at s/D =1.2–1.8, flip-flopping flow at s/D =2-2.4, hybrid flow at s/D =2.5, and antiphase flow at s/D =2.7–5. Mishra et al. (2021) carried out a numerical investigation using the method of stabilized finite-element computations of a two-dimensional (2D) steady laminar flow around a cylinder symmetrically placed in an extremely narrow channel. Whatever Reynolds number values in the range between Re = 4 and Re = 400, the imposition of a blocking rate equal to 0.9 delays the appearance of the adverse pressure gradient along the cylindrical surface. The separation of the laminar boundary layer occurs only at $\mathrm{Re} = 27.8$. The wake of the flow varies in a non-linear way with the Reynolds number. The works above are studies on flows around not very complex geometries. In this context, the present work deals with a numerical analysis on a three-dimensional laminar steady state around an isolated ideal cell of a metallic foam with a geometrical configuration completely different from those presented in the literature review. To our knowledge, the geometric aspect of the metal foam cell has not been used as an obstacle to the supposed three-dimensional flow in steady state. To this purpose, we study the effect of the Reynolds number on the topology of the streamlines and the wake of the flow behind the cell in the Reynolds range $75 \le \mathrm{Re} \le 500$. Then we describe the distribution of the pressure coefficient and the drag coefficient along the periphery of the fibers.

2. MATHEMATICAL FORMULATION OF THE PROBLEM2.

2.1 Physical Model

It consists of a parallelepiped channel (lxhxw) in which an open cell of a metallic foam type cellular material is interposed according to the model proposed by Lu et al (1998). The dimensions values of the channel are $L_x = 47\ D_p$, $L_y = 5.9\ D_p$ and $L_z = 9.7\ D_p$. The cell has a cubic form with a porous diameter of 3.4 mm. The fibers constituting the edges are cylindrical, each with a diameter $D_f = 0.4$ mm. Porosity (ε) , the pore diameter (D_P), and the diameter of the fiber , characteristics of the cell geometry, are related by Eq. 1 given by Bhattacharya et al. (2002).

$$\frac{D_f}{D_p} = 2\sqrt{\frac{1-\varepsilon}{3\pi}} \cdot \frac{1}{G} \tag{1}$$

G is a form factor that takes into account the variation of the ligament cross section with porosity. It is given by the Eq. 2

$$G = 1 - e^{-(1-\varepsilon)/0.04} \tag{2}$$

The cell is positioned at the coordinates $x = 20D_P$, $y = 0$,and $z = 4.18D_P$ as shown in Fig. 1. It constitutes, in this case, an obstacle to the flow assumed to be laminar and steady state

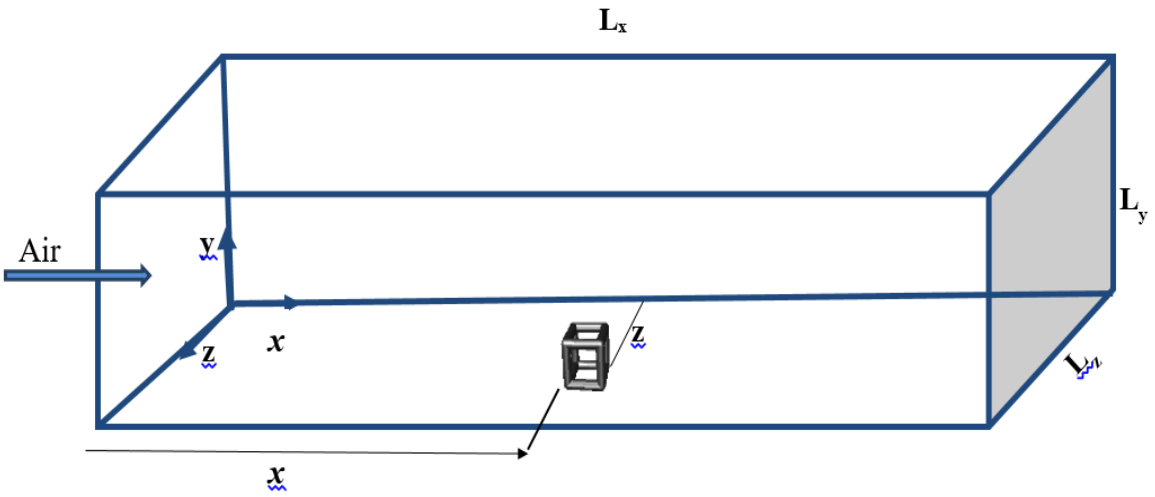

Fig. 1 Geometrical configuration of the physical system

2.2 Governing Equations and Boundary Conditions

The fluid enters through the left of the channel and flows in the channel to the cubic foam located at a distance from the inlet. It interacts with the foam and flows to the outlet of the channel. The fluid considered is air, which is supposed to be incompressible. In this case, the calculated Mach number ($Ma \approx 0.0063$) is too lower than 0.3. This assumes that air is an incompressible fluid. It enters the channel at an ambient temperature and a uniform velocity u_0 . The following assumptions are also adopted:

- The laminar regime is in a steady state.

(In the Reynolds number $Re = \frac{\rho u_0 D_p}{\mu}$, the velocity u_0 is that of the flow at the entrance to the channel. It remains constant during the flow. The dynamic viscosity of the air calculated at T=300K is $1.789.10^{-5}$ *kg/m.s*. It also remains constant during the flow process. For the range of Re in this study (Madani et al. 2007) through out an extensive literature study show that the regime in this case is laminar steady.

- The volume forces are negligible.

Based on these assumptions, the dimensionless three-dimensional continuity and Navier-Stokes equations governing the flow past the cell foam may be written as given by Eqs. (3, 4):

$$\frac{\partial U_i}{\partial X_i} = 0 \tag{3}$$

$$\frac{\partial (U_i U_j)}{\partial X_j} = -\frac{\partial P}{\partial X_i} + \frac{1}{\mathrm{Re}} \frac{\partial^2 U_i}{\partial X_j^2} \tag{4}$$

The dimensionless variables used in these equations are given by Eqs 5:

$$X = \frac{x}{D_P} \ , \ Y = \frac{y}{D_P} \ , Z = \frac{z}{D_P} \ , \ U = \frac{u}{u_0} \ , \ V = \frac{v}{u_0} ,$$

$$W = \frac{w}{u_0} \text{ and } P = \frac{p}{\rho u_0^2} \tag{5}$$

U_i : the three Cartesian velocity components (U ,V ,W) along the X,Y and Z directions ; D_P : diameter pore; u_0 : inlet velocity supposed to be the characteristic velocity ; ρ : *the* density of the fluid. The Reynolds number based on pore diameter of the metal foam cell is given by Eq. 6

$$\mathrm{Re} = \frac{\rho u_0 D_P}{\mu} \tag{6}$$

The boundary conditions used are written as follows Eqs (7-12):

- **Inlet** : $(U,V,W) = (1,0,0)$ (7)
- **outlet** : pressure outlet $P = 0$

$$\frac{\partial U}{\partial X} = \frac{\partial V}{\partial X} = \frac{\partial W}{\partial X} = 0 \tag{8}$$

- **Canal walls**:

- Upper and lower walls at $Y = 0$ or $Y = \frac{L_y}{D_P}$

$U = V = W = 0$ (adherence at the walls) (9)

-Side walls at $Z = 0$ or $Z = \frac{L_z}{D_P}$ $U = V = W = 0$

(adherence at the walls) (10)

Cell edges:

- $U = 0$ (Adherence at edges in longitudinal direction x) (11)

- $V = W = 0$ (Edges are points of stagnation in the flow.) (12)

3. NUMERICAL PROCEDURE

Dimensionless equations (3) and (4) associated with boundary conditions (7–12) are solved using the Ansys Fluent 18.2 software. A grid distribution scheme produced by the ICEM CFD software is used to generate a structured grid of hexahedral for control volumes and quadratic for faces (Fig. 2). We adopted the "Standard" scheme for pressure interpolation. The space discretization of the diffusive-convective terms is of the second "UPWIND "type. The link between the pressure and the velocity fields is assumed by the SIMPLE (Semi-Implicit Method for Pressure-Linked Equations) algorithm. The under-relaxation coefficients are 0.3, 1.1, and 0.7 for pressure, density, and momentum, respectively. The convergence criteria for the continuity equation and the velocity components are 10^{-6}.

4. MESH INDEPENDENCE AND VALIDATION

In order to ensure the independence of the numerical solution with respect to the mesh, we analyzed the effect of four meshes, one on the drag coefficient and the other on the maximum pressure coefficient along the upper upstream transverse fiber (Table 1). As it can be seen in Table 1, the variation decreases as the mesh becomes denser. The percent variation of the drag coefficient decreases by 0.03% between mesh 2 and mesh 3, and by 0.005% between mesh 3 and mesh 4. The percent variation of the maximum pressure coefficient (stagnation) diminishes by 0.026% between mesh 2 and mesh 3, and by 0.005% between mesh 3 and mesh 4. Therefore, mesh 2 is adopted in this study because the deviations of drag and stagnation pressure coefficients for this mesh and other meshes are very small. Furthermore, this mesh (M.2) occupies less space in the computer's memory. Consequently, the convergence of the iterative process is accelerated and the simulation time is much reduced

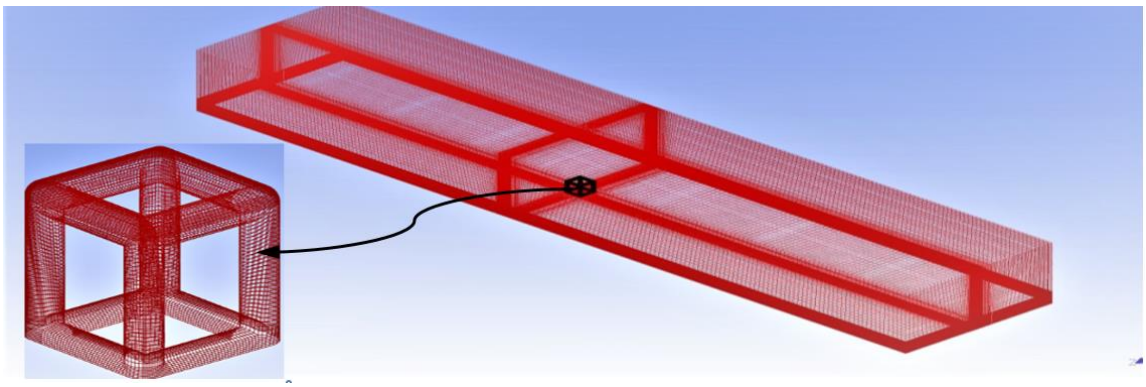

Fig. 2 Mesh distribution of the physical model

Table 1 Effect of grid density on grid independence

	Number of cells	Number of nodes	C_D	$C_{p.max}$	$\lvert\Delta C_D\,\%\rvert$	$\lvert\Delta C_{P.max}\,\%\rvert$
Mesh 1	1801345	1853347	0.91297	1.93007		
Mesh 2	1975785	2031547	0.91392	1.93062	0.104	0.028
Mesh 3	2150225	2209747	0.91420	1.93010	0.030	0.026
Mesh 4	2387947	2387947	0.91415	1.93000	0.005	0.005

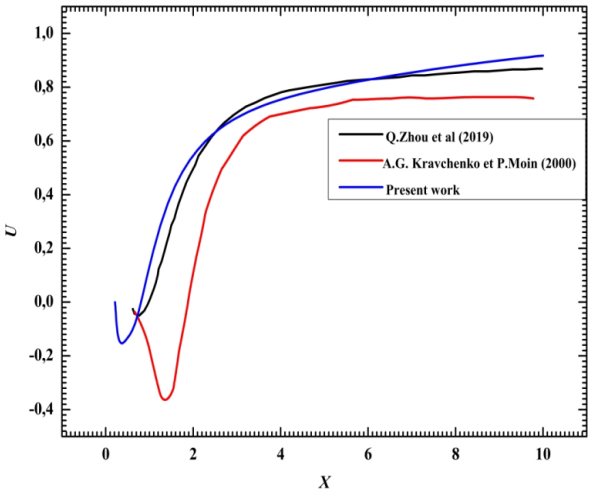

Fig. 3 Comparison of the longitudinal velocity with those calculated by Zhou et al. (2019) and Kravchenko and Mon (2000)

The percentage variation is given by Eq. (13)

$$\left|\Delta\%\right| \text{(percentage variation)} = \left(\frac{|V_C - V_P|}{V_P} \times 100\right) \qquad (13)$$

Where V_C and V_P successively represent the current values and previous values.

In order to validate the code calculation, we resort to the cylindrical bodies in tandem, as the geometry of the metallic foam cell in the present study is entirely absent in the bibliography of three-dimensional flow physics. The studies of Zhou et al. (2019) and Kravchenko and Moin (2000), have been employed to validate our numerical simulation model. Zhou et al. (2019) investigate the three-dimensional flow over two tandem circular cylinder at $Re = 10^3$ and L/D (spacing ratio) $= 1.25 - 6$. Kravchenko and Moin (2000) studied numerical simulations of flow past a circular cylinder at a subcritical Reynolds number, $Re_D = 3900$ using the technique of large eddy simulation. Figure.3 compares the dimensionless longitudinal velocity U of the two references with that of the present study. It seems clear that the curve of the present work evolves in a more quantitative and qualitative way than those of the comparison references. Zhang et al. (2022) examined an experimental and numerical study of three-dimensional flow around two tandem cylinders arranged vertically in the flow. The physical evolution of the curve given in this work look like qualitatively and quantitatively that given by the above reference (Fig. 4)

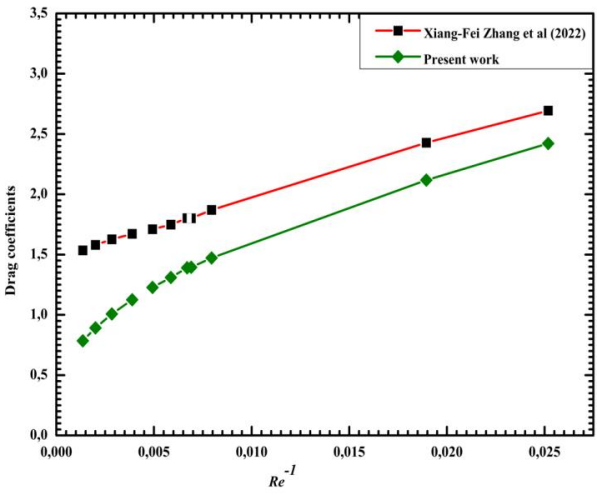

Fig. 4 Comparison of the drag coefficient

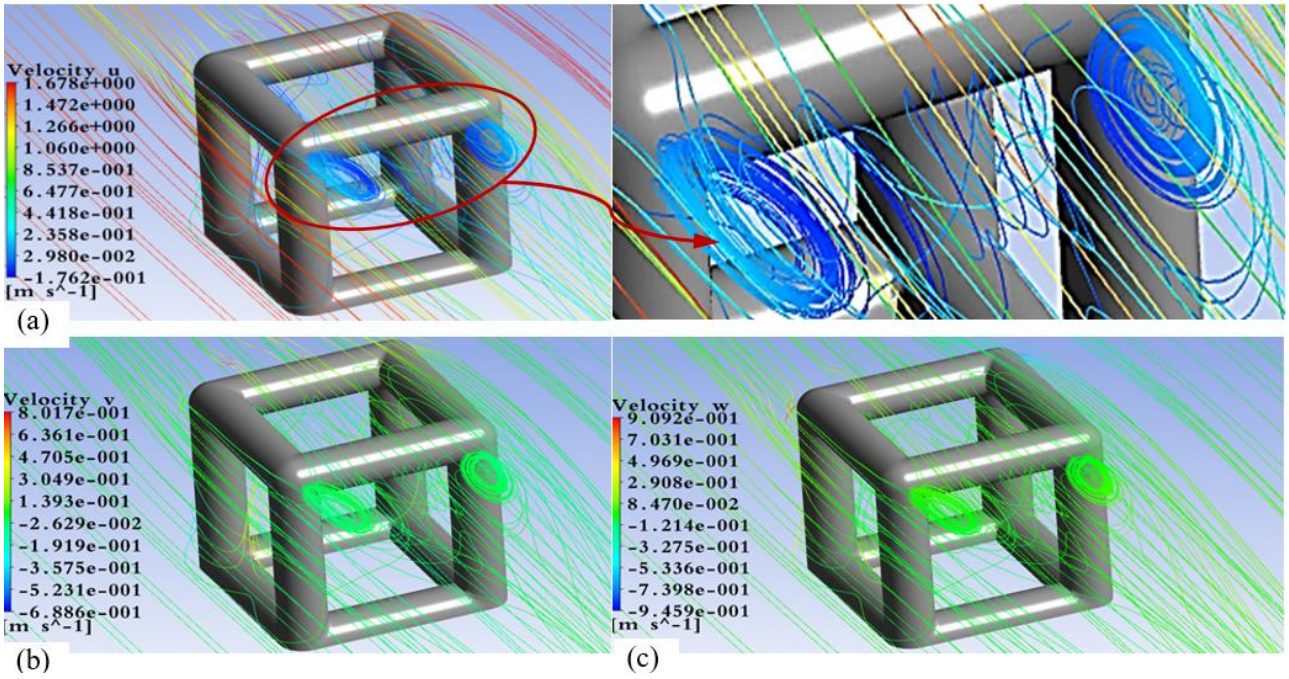

Fig. 5 Three-dimensional perspective of velocity components: (a) u, (b) v and (c) w for Re=300

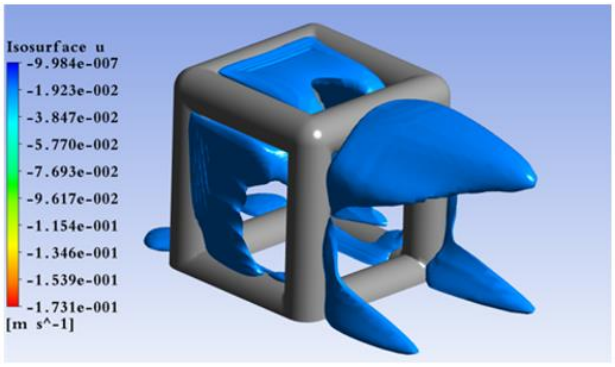

Fig. 6 Iso-surface of the longitudinal velocity u, for Re=300

5. RESULTS AND DISCUSSION

In this section, we present the results obtained according to the structure of the streamlines. These results are completed by the drag coefficient, the pressure coefficient, the saddle point, and an analysis of the effect of the porosity of the foam ($\varepsilon = 0.88$, $\varepsilon = 0.90$, $\varepsilon = 0.92$ and $\varepsilon = 0.94$)on the longitudinal velocity. The numerical simulations were carried out in Reynolds range $75 \le Re \le 500$.

5.1 Three-Dimensional Perspective Flow

Figures 5 shows a three-dimensional perspective illustration of the velocity component's streamline distribution around and inside the metal foam cell for Re = 300. The streamlines deform in the third dimension due to the shear of the flow caused by the vertical and horizontal fibers. The trajectories separate upstream of the horizontal fiber in contact with the flow and then describe spiral-type vortex zones downstream of the second horizontal fiber and near the fibers parallel to the flow. It should be noted that the gaps delimited by the upper fibers and the lateral fibers affect the structure of the flow because vortex zones are created in these locations due to the stagnation effect generated by the fibers of the cell.

It is clear that the upper and lateral fibers, located respectively at $y = D_P$ and $z = 5.3D_P$ planes, considerably modify the shape and value of the flow structure, particularly in the gaps and wake of the metal foam cell. The iso-surface of u; the x component of the velocity is given in Fig. 6; it corroborates the results presented above.

5.2 Flow Structure in Plane $z = 5,3D_P$ (Middle Of Right Cell Fibers)

In Figs 7, we analyze the effect of Reynolds numbers (Re = 75, Re = 275, Re = 350, and Re = 500) on the streamlines distribution at $z = 5,3D_P$. At Re = 75 (Fig. 6a), in the sector of the first upper corner, the values of the streamlines shaped similar to a parabola decrease as they approach this corner, reflecting the appearance of localized vortices, particularly in the vicinity of the upper fiber. Under the effect of the adverse pressure gradient, a separation node D is noted at coordinates $(x, y, z) \approx (21.15D_P, 0.549D_P, 5.3D_P)$ for Re = 275 (Fig. 6b). Above this point, the axially curved lines contain a vortex zone that extends, approximately $0.38D_P$ in the wake. Below the same point, another recirculation zone is formed and tends to extend, particularly as it approaches the point of reattachment R. An arc-shaped vortex roll is established in the lower downstream corner due to the interaction of the reversal flow and the latter. At Re=350 (Fig. 6c), the streamlines detach at coordinates $(x \approx 21.35D_P, y \approx 1.05D_P)$, located at the trailing edge of the horizontal fiber. The shear layer wraps around in the wake and forms a first spiral-shaped vortex structure that is arranged at the top, behind the downstream fiber. This

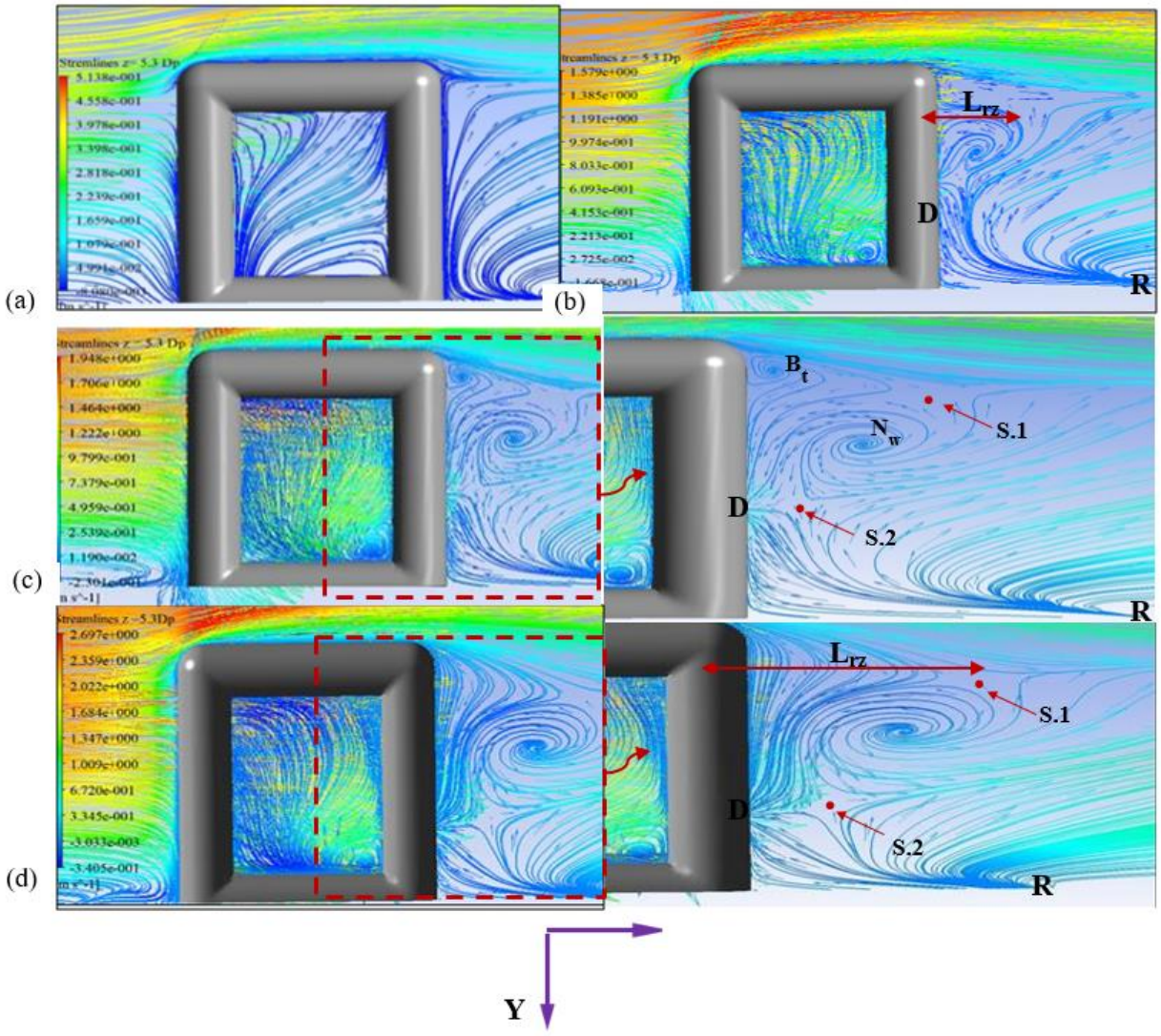

Fig.7 Streamlines in plane at z=5.3 D_P (a) Re=75, (b)=275, ,(c)=350,(d)=500

aspect of this structure is named B_t by Krajnović (2011) and Sumner et al. (2017). Vortex B_t is that it is the mean flow field in the vertical $z = 5{,}3D_P$ symmetry plane, which typically presents a vortex with its focus point downstream of the trailing edge. A second spiral structure composed of a counterclockwise vortex, named N_w by Krajnović (2011), develops from the separation point D. N_W Vortex is associated with the presence of a saddle point in the symmetry plane, which separates downwash-dominated and upwash-dominated flow regions, Vortex N_W is therefore a consequence of the presence of this saddle point and of the existence of upwash**.** A saddle point S.1 detects the two vortex zones and the downwash and upwash of the flow located in the upper half-plane. The saddle point S.2, which manifests at coordinates $(x, y, z) \approx (21.29D_P, 0.47D_P, 5.3D_P)$, is attributed to the interaction of the downwash flow coming from the vortex **N_w** and the upwash flow located in the lower half-plane of the wake. The separation point (D) moves down to the coordinate $y \approx 0.43D_P$. At Re=500 (Fig. 6d), the separated flow force is stronger; the separated flow region at the trailing edge, at coordinates $(x, y, z) \approx (21.07D_P, 1.11D_P, 5.3D_P)$ extends further and pushes the saddle point S.1 approximately $0.294D_P$ into the wake. The saddle point S.2 is located at $y = 0.34D_P$, at Re = 500. It moves downward by $0.13D_P$ in the Reynolds range $350 \le \mathrm{Re} \le 500$ due to the weakness of the upwash.

Within this context, Zhang's work demonstrates that the saddle point reaches its maximum ($Y = 0$) at the same Re number (Re = 500). Despite the slowness of S.2, the representative profile of the saddle point S.2 as function of Re (Fig. 8) varies similarly to the curves reported by Zhang et al. (2017) and Zhao et al. (2021). As a result, the vertical fibers of the cell behave similarly to tandem cylinders since the wake characterized by the saddle point S.2 retains a topography very similar to that of the cylinders arranged in tandem. Furthermore, the appearance of the wake sector generated by saddle point S.1 is entirely distinct from the wake configuration of other geometries that we have consulted in numerous biographical works. This represents a characteristic of the cell.

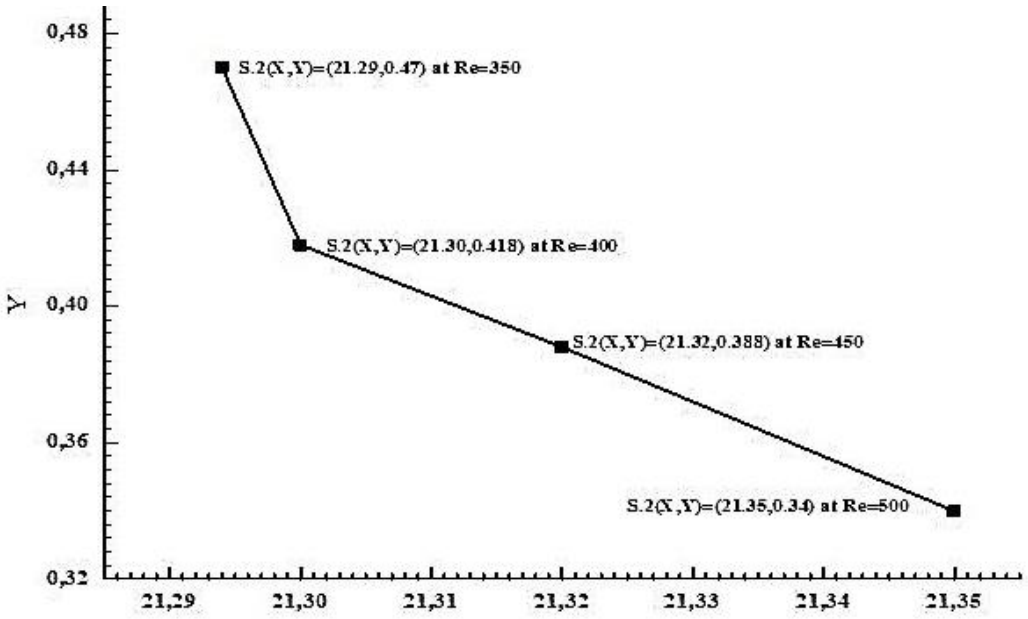

Fig. 8 Displacement of the saddle point S.2 in the wake as a function of Re

5.3 Flow Structure in Plane $y = D_P$ (Middle of Upper Cell Fibres)

Figures. 9 shows the effect of Reynolds number (Re=75, Re=275, Re=350, and Re=500) on the streamlines distribution at $y = D_P$. At Re = 75, the saddle point S.$_{gap}$, which appears in the gap at coordinates $(x, y, z) \approx (20.33D_P, D_P, 4.85D_P)$ configures two upwash and downwash flows and two symmetrical, uniform, and stable zones where recirculation is almost non-existent. The detachment of the streamlines downstream creates a pair of arch-shaped vortices centralized at focal points $(x \approx 21.17D_P, z \approx 4.47D_P)$ and $(x \approx 21.16D_P, z \approx 5.23D_P)$. In the wake, the separation lines S.l.1 and S.l.2 completely isolate the two recirculation zones from upwash and downwash flow. Hence, the saddle point appears at $(x, y, z) \approx (21.17D_P, D_P, 4.85D_P)$. As Re increases from 275 to 350, shear layers create two symmetrical recirculation bubbles or vortices in the wake of the two numbers of Re. The upper recirculation, clockwise in direction, displays negative vorticities. Whereas the lower recirculation, counterclockwise in direction, exhibits positive vorticities. Streamlines reveal that there is no fluid exchange between the two recirculation bubbles. For Re = 500, the evolution of the longitudinal velocity versus the transverse direction shows an asymmetry between the two bubbles (Fig. 10). The F2 focus has moved by 0.096 Dp relative to the F1 focus. The upper recirculation bubble is stronger than the lower recirculation bubble. The streamline profiles illustrate that fluid particles move from the lower bubble to the upper bubble, indicating a transfer of matter between the two vortices. The longitudinal distribution of recirculation bubbles conforms globally to those reported by Palau-Salvador (2008) in the case of a flow over two tandem cylinders, in which one cylinder is located downstream of the other. Two symmetrical recirculations with oval shapes are located within the gap. Above the midline, they contain negative vorticities in the clockwise direction. Below, positive vorticities are present in the counterclockwise direction. There is no interaction between the two counter-rotating cells as Re increases. The saddle point S.1 indicates a minimal displacement that is worth 0.18 D_P in the $75 \leq \text{Re} \leq 500$ range.

Increasing Re does not influence the structure of the streamlines because the fibers lock in the development of the flow. In the same interval of Re, the saddle point S.2 indicates a displacement $(x_{S.2})$ of $1.74D_P$ in the wake, which is 9.65 times that marked by S1 in the gap, according to the curve in Fig. 11. Contrary to the flow around tandem cylinders (Li et al., 1991; Shang et al., 2019; Afgan et al., 2023) the flow configuration in our case does not show any vortex shedding in the wake within the Reynolds range. In this steady state case $\left(\frac{\partial}{\partial t} = 0\right)$ the strouhal number St=0. Therefore, shedding frequency $f = 0$. This means that vortex shedding does not occur around the porous cell.

6. PRESSURE COEFFICIENT

Along the ABCD circumference, located on the lateral fibers of the cell, in the graphical configuration Fig. 12, the pressure coefficient evolution is plotted along LD/Dp at z = 5.3 Dp for four values of Reynolds number (Re = 75, Re = 250, Re = 350, and Re = 500). As can be seen, the stagnation effect of the vertical fiber AB reduces the pressure coefficient Cp by 32.55% in the Reynolds range. The fluid movement is increased by the curvature of the fiber AB, leading to a sudden decrease in the pressure coefficient. Beyond point B, the flow decelerates and causes an increase in the curve up to the vicinity of point C, where it undergoes a minimal decrease until reaching negative values, which reflect the separation of the

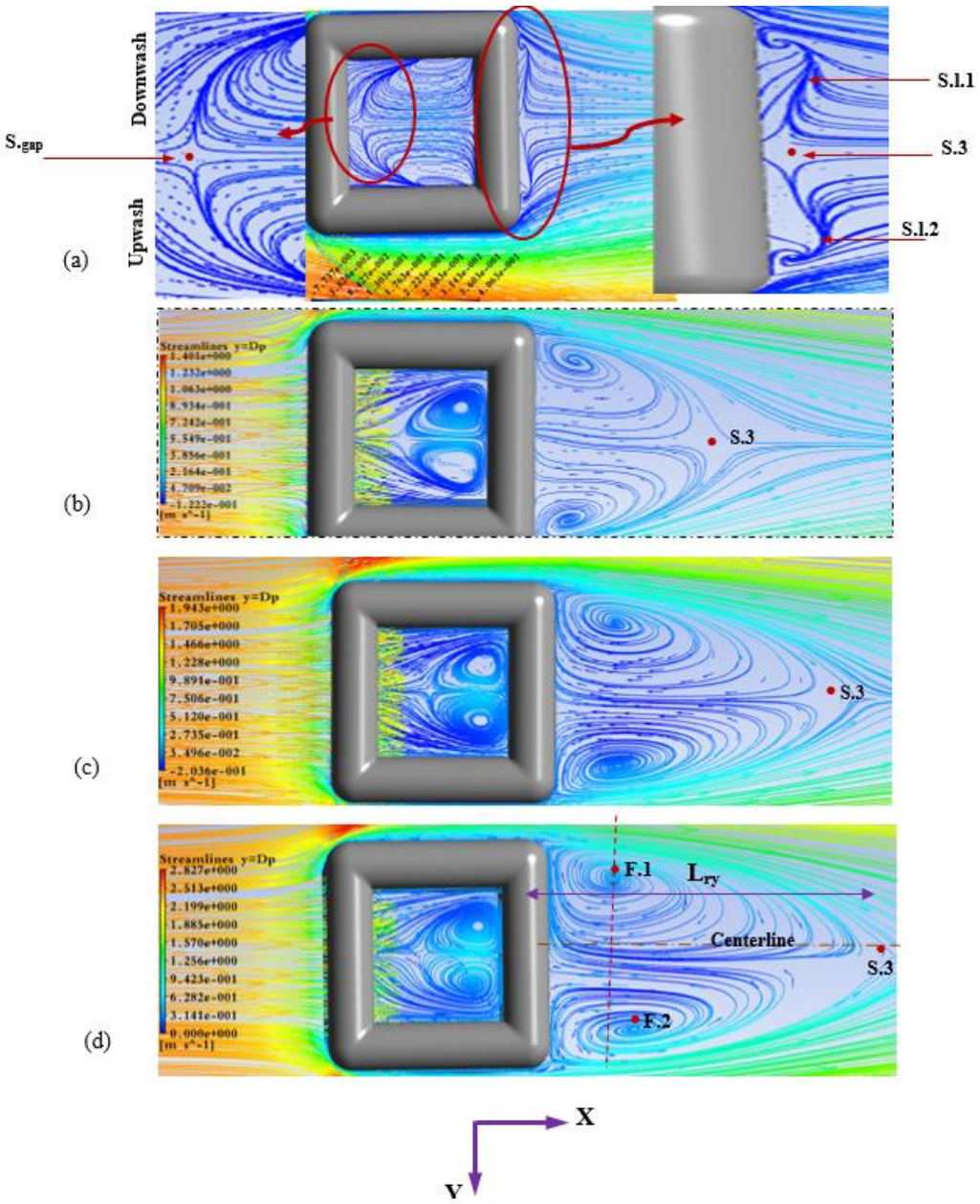

Fig. 9 Streamlines in plane at y= D_p (a) Re=75, (b)=275, (c)=350, (d)=500

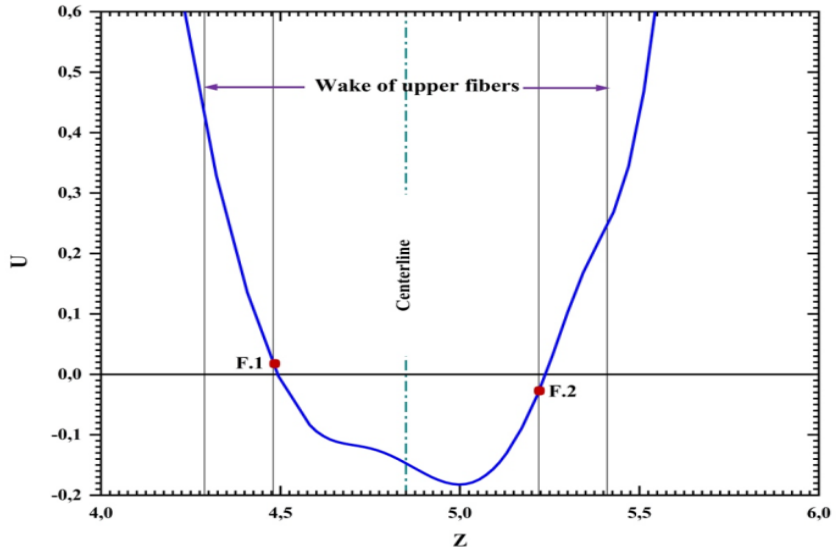

Fig. 10 Longitudinal velocity along the transverse direction Z passing through F.1

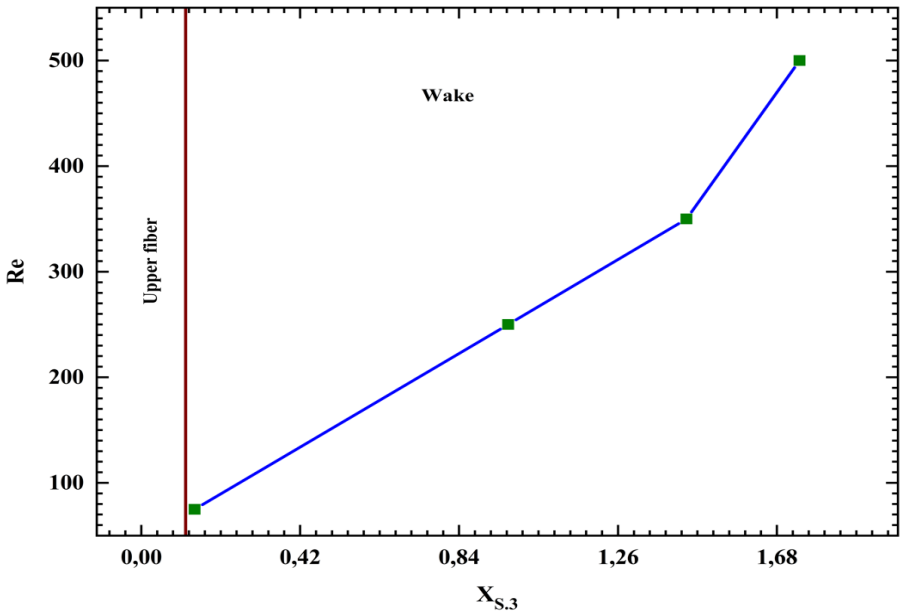

Fig. 11 Displacement of the saddle point S.3 in the wake as a function of Re

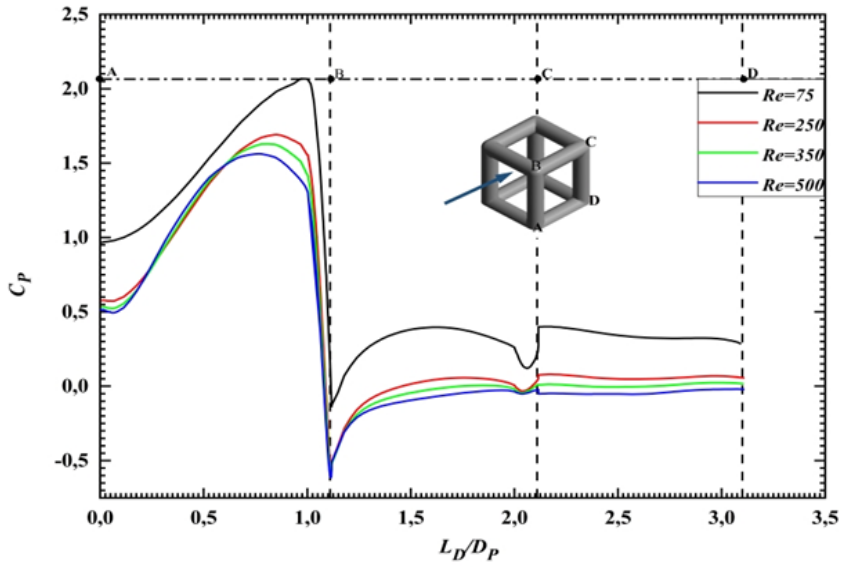

Fig. 12 C_P **versus** L_D/D_P **(**$L_D = L_{A\to D}$**, at** $z = 5.3D_P$**), in the range** $75 \le \mathrm{Re} \le 500$

streamlines at this location. Despite showing very limited growth, the profile remains generally linear along the CD fiber. The Reynolds effect on the flow structure behind the CD fiber is almost negligible. The evolution of the pressure coefficient is qualitatively in accordance with the curve reported by Richards et al. (2001) and Haupt et al. (2011). The contours clarify the evolution of the pressure coefficient, particularly in the wake. At Re = 75, this coefficient shows positive values in the fiber curvature downstream (Fig. 13). Consequently, no separation is marked, and the streamlines remain attached to the CD fiber, as shown in Fig. 7.a. The growth of the pressure coefficient in the wake generates minor recirculations, which remain localized in the immediate vicinity of point D. Negative pressures become more apparent as the Reynolds number increases (Zhang et al., 2017). At Re=500, negative values become more pronounced, particularly in the upwash and downwash sectors located upstream of saddle point S.2, as shown in Fig. 14.

Figure 15 illustrates the effect of Reynolds number (Re=75, Re=250, Re=350, and Re=500) on the evolution of the pressure coefficient versus L_D/D_p, at y=Dp. This figure shows that this coefficient increases as the Reynolds number decreases. The parabolic profile on the periphery AB indicates that the pressure coefficient reaches its maximum values due to the effect of stagnation of the upstream transverse fiber AB (Table 2).

The unblocking of the fluid particle flow at curvature B favors the inertial effect. Consequently, the pressure coefficient decreases sharply until it reaches negative values. The favorable pressure gradient away from the cell contributes to the growth of the pressure coefficient on the lateral sides of the BC and DA fibers. The profile marks a slight decrease in the curvatures C and D, then linearizes

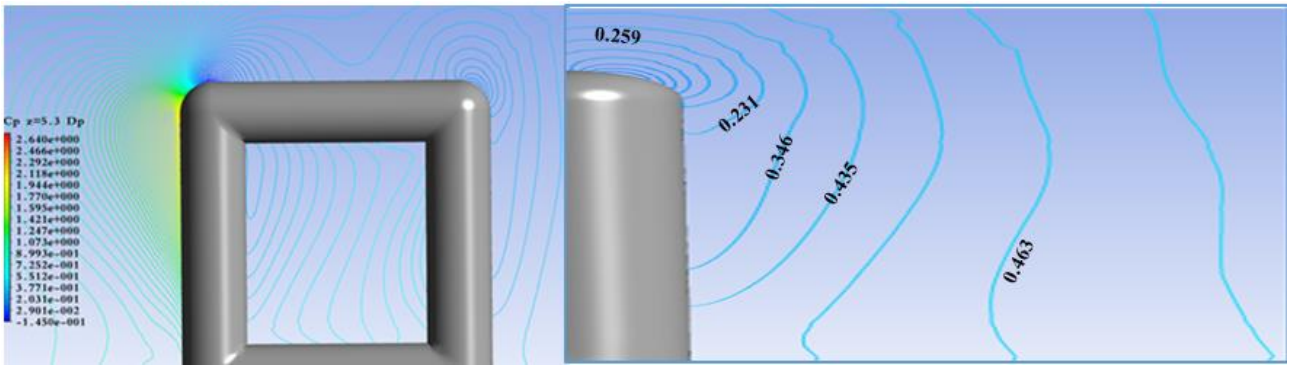

Fig. 13 Contours of pressure coefficient in plane C_P at Re=75

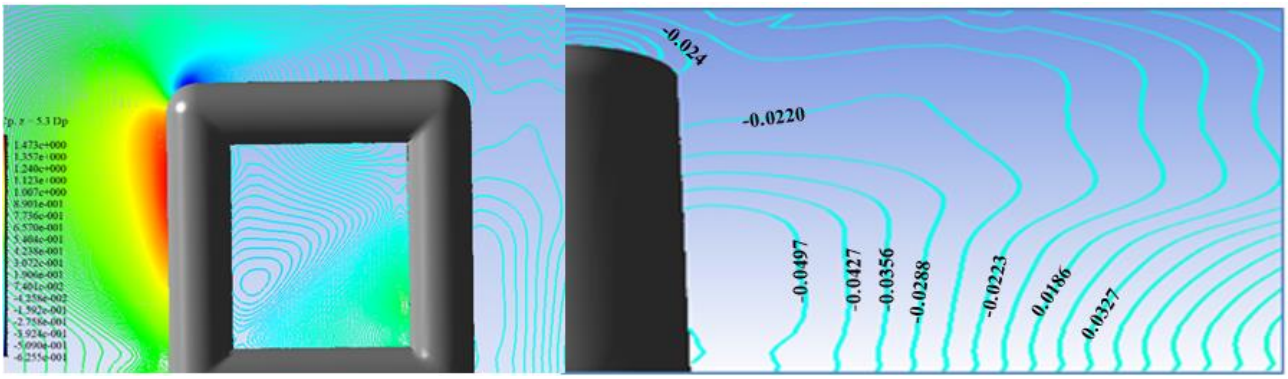

Fig. 14 Contours of pressure coefficient in plane C_P at Re=500

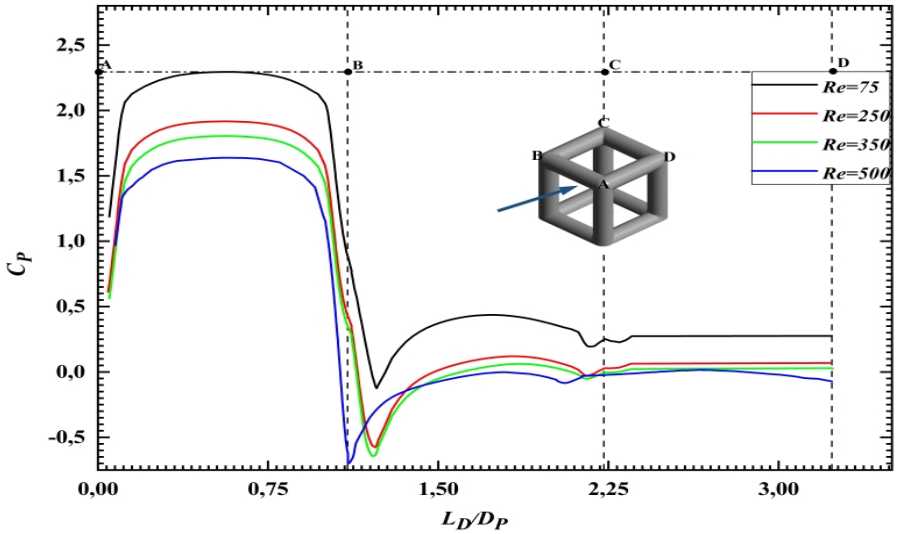

Fig. 15 C_P versus L_D/D_P ($L_D = L_{A\to D}$, at $y = D_P$), in the range $75 \le Re \le 500$

Table 2 Maximum values of the pressure coefficient along the upstream horizontal fiber

Re	L/D_p	$C_{P.max}$
75	0.543	2.294
250	0.574	2.069
350	0.543	1.916
500	0.543	1.637

on the rest of the periphery of the fiber CD. The curve of the pressure coefficient as a function of Reynolds, represented Fig. 15, illustrates a good qualitative agreement with the work completed by Hu et al (2018) and Paterson & Apelt (1990). At Re = 75, the contours decrease in the perimeter of the curvature C due to the reattachment of the streamlines (Fig. 16). Downstream of the CD fiber, the pressure coefficient increases slightly. Hence, a saddle point appears in the sector surrounding the downstream fiber. The increase in Reynolds (Re = 500)

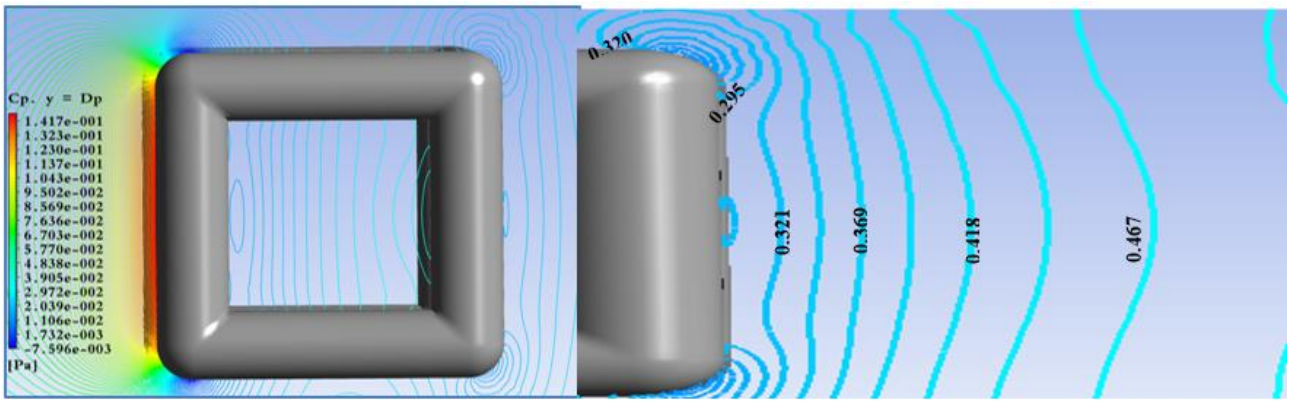

Fig. 16 Contours of the pressure coefficient in plane $y = D_P$ at Re=75

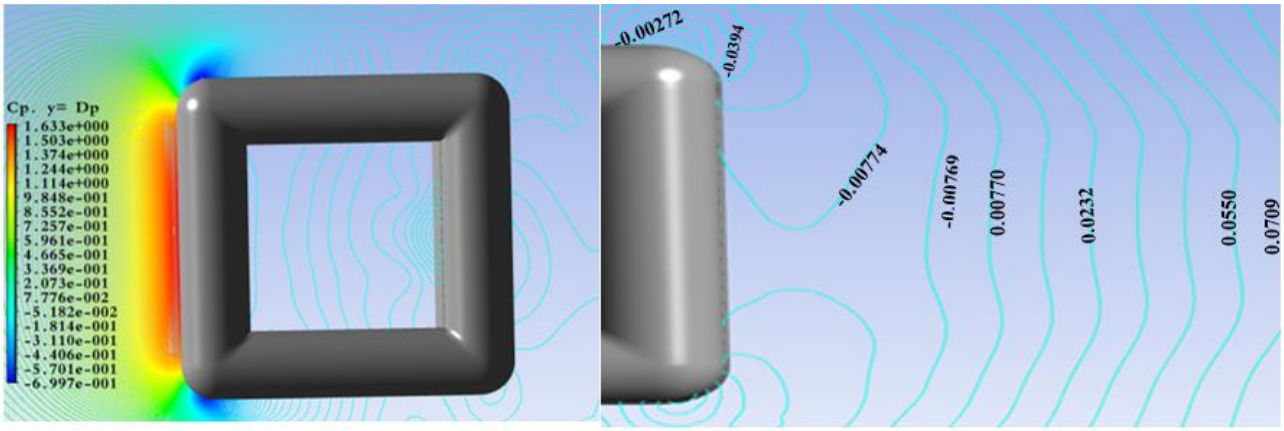

Fig. 17 Contours of pressure coefficient in plane $y = D_P$, at Re=500

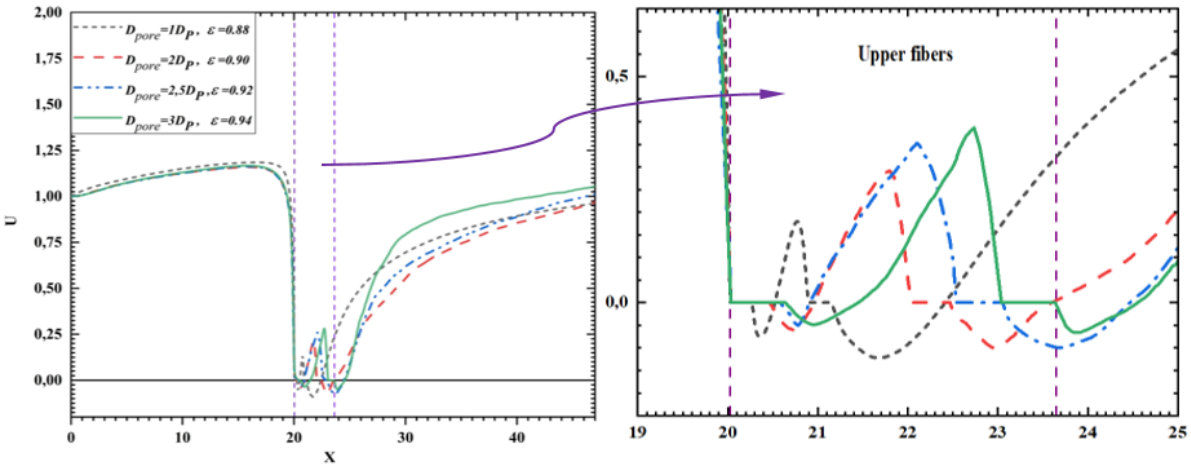

Fig. 18 Evolution of the longitudinal velocity with pore diameter

generates negative values at the curvature C, thus marking the separation of the flow. As shown in Fig. 17, the contours mark a growth in the wake until the coordinate x = 21.67 D_P.This causes the saddle point to move within the wake.

7. EFFECT OF OF THE FOAM PORE DIAMETER ON THE LONGITUDINAL COMPONENT VELOCITY

Figure 18 illustrates the evolution of the longitudinal component velocity versus X in the middle of the upper fibers plane of the cell. The values considered, $1D_P$, $2D_P$, $2.5D_P$, and $3D_P$ correspond to the respective porosities $\varepsilon = 0.88$, $\varepsilon = 0.90$, $\varepsilon = 0.92$, and $\varepsilon = 0.94$. Mostly unperturbed upstream, the flow stagnates completely at the fibers for all pore diameter values (D_{pore}). In the gap of the upper fibers, the profiles decrease as the pore diameter decreases. It is therefore clear that the strength of backflow weakens as the pore diameter increases. This result qualitatively agrees with the one obtained by Saha (2004). It is observed in the case $D_{pore} = 2.5D_P$, and

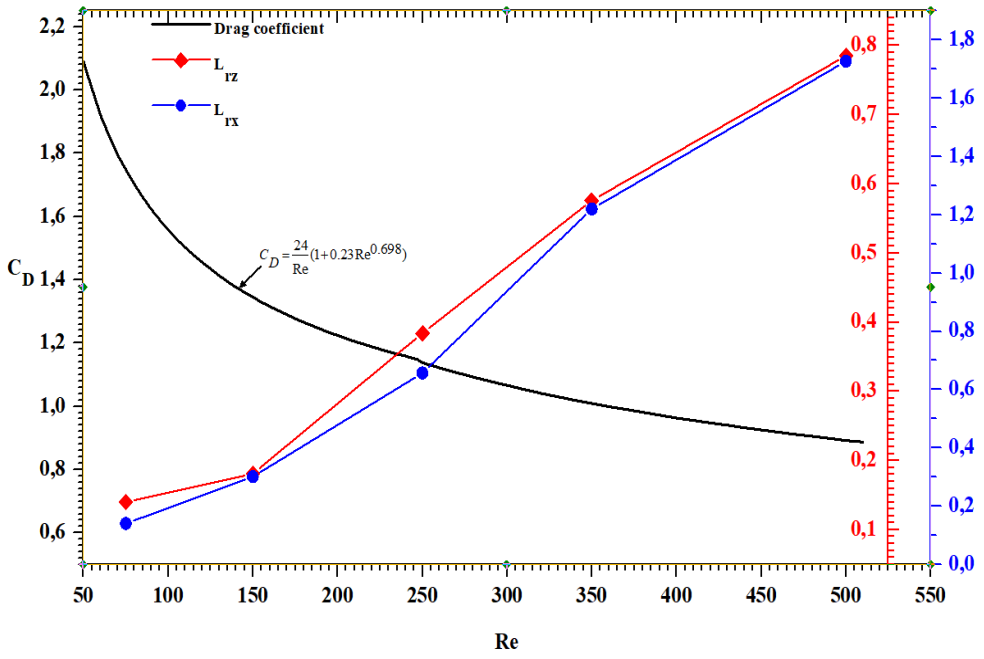

Fig. 19 Evolution of drag coefficient C_D and recirculation length (L_{rz} , L_{ry}) vs Re

$D_{pore} = 3D_p$ a small decay near the downstream fiber. Hence, the appearance of less recirculation zones favors the recovery of the velocity downstream of the cell.

8. EFFECT OF Re ON THE DRAG COEFFICIENT

The drag coefficient decreases significantly as the number of Reynolds increases for Re values $\mathrm{Re} \le 120$ and continues to decrease until $\mathrm{Re} = 270$, then reaches almost constant values as Re increases (Fig. 19). This evolution highlights the stability of the drag coefficient values. The drag coefficient decreases because the viscous forces weaken as the Reynolds number increases. This contributes to the reduction of the boundary layer thickness, which consequently leads to the reduction of the drag coefficient. These results are in agreement with those reported by Saha et al. (2004) and Clift et al. (2013). These latter report mathematical relations, reflecting the evolution of the drag coefficient, of the following form $C_D = \frac{24}{\mathrm{Re}}(1 + a\mathrm{Re}^b)$ where a and b are constants. In the present work, the coefficient a and b are estimated to be equal to 0.23 and 0.698 respectively. For the coefficients $a = 0.125$ and $b = 0.72$, Clift et al. (2013) report a similar equation representing drag coefficient in the wake of the sphere for Re <1000 .The range deviation between the two equations varies approximately from 28.68 % to 35.59%. The drag force is a consequence of the flow, since it is related to the momentum deficit in the wake. It appears that the structure of the wake, particularly the recirculation zones, leads to a specific value of the drag soefficient. Figure 19 shows clearly the existence of a relationship between the recirculation lengths L_{rz} and L_{ry} , located respectively in the wake of planes $z = 5.3D_P$ and $y = D_P$ (Fig. 7.d and Fig. 9.d), and the drag coefficient. At the periphery of the downstream lateral and transverse CD fibers located in the respective planes $z = 5.3D_P$ and $y = D_P$ (Figs 12 and 15), the low pressure associated with the Reynolds number creates recirculation zones. Recirculation lengths are inversely related to the drag coefficient. In other words, an increase in recirculation lengths signifies a decrease in the drag coefficient. These recirculations reduce the drag coefficient in equal proportion (51%) in the range $75 \le Re \le 500$, although L_{ry} is 2.2 times L_{rz} . It appears that the wake of the lateral fibers of the z=5.3Dp plane contributes better to the drag coefficient.

This study shows that the predominance of downwash associated with the instability of saddle point S.2 in the wake when Re increasing leads to a decrease in the drag coefficient in the wake.

9. CONCLUSION

The present work is aimed on a numerical study of a three-dimensional, steady flow in a laminar regime around a cell of metallic foam of cubic shape disposed in a horizontal channel. Dimensionless Navier-Stokes equations are resolved using the Ansys Fluent 18.2 software. The effects of the Reynolds number and porosity of the foam on the streamlines distribution and the aerodynamic coefficients are deeply analysed. The main results are summarized as follows .The three-dimensional perspective flow configuration reveals that the streamline structure is notably altered by the upper and lateral fibers located at $z = 5.3D_P$ and $y = D_P$.

- At $z = 5.3D_P$ (**lateral fibers**)

- A clockwise spiral vortex named Bt by Krajnovic is generated by the rolling-up of the shear layer from $\mathrm{Re} = 275$. Below, a downwash is formed by counter-rotating vortices named Nw, which is developed from the separation point D. The interaction between the base vorticity and the wall boundary layer creates upwash.

- The saddle point moves downward by $0.13D_P$ in the Reynolds range $350 \le \mathrm{Re} \le 500$ due to the weakness of the upwash. This displacement is comparatively slow compared to the findings by Zhao et al. (2021) , where the saddle point reaches its maximum at the lower wall (Y = 0). This corresponds to the complete disappearance of the upwash at the same Reynolds number (Re = 500). As a result, the lateral fibers of the $z = 5.3D_P$ plane significantly retard the disappearance of the upwash, despite the fact that the general appearance of the wake largely resembles that of the cylinders arranged in tandem.

- At $y = D_P$ **(upper fibers)**

- Two saddle points S.1 and S.2 mark the respective appearance of two recirculation bubbles in the gap and the wake. Point S.2 extends $1.74D_P$ into the wake, i.e., 9.65 times the gap displacement of S.1. The wake configures two flow distributions:

  - A stationary and symmetrical flow when $\mathrm{Re} \le 500$. Stationary, asymmetrical flow when $\mathrm{Re} \ge 500$.

- Compared with flows around cylinders arranged in tandem, the vortex shedding is completely absent in the wake of the cell due to the steady-state.

- The decrease in pore diameter favors recirculation in the cell gap

- An increase in recirculation lengths (L_{rz} and L_{ry}) implies a decrease in the drag coefficient. These recirculations reduce the drag coefficient in equal proportion (51%) in the range $75 \le Re \le 500$, although it is 2.2 times . It appears that the wake of the lateral fibers of the z=5.3Dp plane contributes better to the drag coefficient.

- We consider that the predominance of downwash associated with the instability of saddle point S.2 in the wake when Re increases leads to a decrease in the drag coefficient in the wake.

CONFLICT OF INTEREST

The author declares that there is no conflict of financial or non-financial interest to disclose.

AUTHORS' CONTRIBUTION

Amroune Abdelhafid: Investigation: Carried out the simulation work; Validation: Validated the simulation results against literature data; Formal Analysis: Analyzed and discussed the results; Writing Original Draft: Prepared the initial manuscript; Writing - Review & Editing: Contributed to manuscript revisions. **Madani Brahim**: Conceptualization: Developed the idea and formulated research goals; Methodology: Designed the mathematical model and numerical resolution method; Software: Selected the software for the study; Formal Analysis: Contributed to the interpretation of results; Resources: Provided data resources; Supervision: Oversaw the research activity planning and execution; Project Administration: Managed and coordinated the research activity; Funding Acquisition: Secured funding for the project.

REFERENCES

Abaidi, A., & Madani, B. (2020). Intensification of hydrogen production from methanol steam reforming by catalyst segmentation and metallic foam insert. *International Journal of. Hydrogen Energy*, *46*(75), 37583-37598. https://doi.org/10.1016/j.ijhydene.2020.12.183

Abu-Qudais, M., Haddad, M. O., & Maqableh, M. A. (2001). Hydrodynamic and heat transfer characteristics of laminar flow past a parabolic cylinder with constant heat flux. *Heat and Mass Transfer*, *37*, 299–308. https://doi.org/10.1007/s002310100199

Afgan, I., Kahil, Y., Benhamadouche, S., Ali, M., Alkaabi, A., Berrouk, S. A., & Sagaut, P. (2023). Cross flow over two heated cylinders in tandem arrangements at subcritical Reynolds number using large eddy simulations. *International Journal of. Heat and Fluid Flow*, *100*(10), 109115. https://doi.org/10.1016/j.ijheatfluidflow.2023.109115

Backer, J. C. (1979). The laminar horseshoe vortex. *Journal of Fluid Mechanics*, *95*(2), 347-367. https://doi.org/10.1017/S0022112079001506

Behera, S., & Saha, K. A. (2019). Characteristics of the flow past a wall-mounted finite-length square cylinder at low Reynolds number with varying boundary layer thickness. *Journal of Fluids Engineering*, *141*(6), 061204. https://doi.org/10.1115/1.4042751

Bhattacharya, A., Calmidi, V. V., & Mahajan, L. R. (2002) Thermophysical properties of high porosity metal foams. *International Journal of Heat and Mass Transfer*, *45*(5), 1017-1031. https://doi.org/10.1016/S0017-9310(01)00220-4

Chen, W., Ji, C., Alam, M. Md., & Yan, M. (2022). Three-dimensional flow past two stationary side-by-side circular cylinders. *Ocean Engineering*, *244*, 110379. https://doi.org/10.1016/j.oceaneng.2021.110379

Clift, R., Grace, J. R., & Weber, M. E. (2013). *Bubbles, drops and particles*. Dover Publications, Incorporated. ISBN 9780486788920, 048678892X

Ferfera, S. R., & Madani, B. (2020). Thermal characterization of a heat exchanger equipped with a

combined material of phase change material and metallic foams. *International Journal of. Heat and Mass Transfer*, *148* (11), 119162. https://doi.org/10.1016/j.ijheatmasstransfer.2019.119162

Haupt, E. S., Zajaczkowski, J. F., & Peltier. J. L. (2011). Detached eddy simulation of atmospheric flow about a surface mounted cube at high reynolds number. *Journal of Fluids Engineering*, *133*(3), 031002. https://doi.org/10.1115/1.4003649

Hu, J., Xuan, B. H., Kwok, S. C. K., Zhang, Y., & Yu, Y. (2018). Study of wind flow over a 6m cube using improved delayed detached Eddy simulation. *Journal of Wind Engineering and Industrial Aerodynamics*, *179*, 463-474. https://doi.org/10.1016/j.jweia.2018.07.003

Hwang, Y. J., & Yang, S. K. (2004). Numerical study of vortical structures around a wall-mounted cubic obstacle in channel flow. *Physics of Fluid*, *16*(7), 2382-2394. https://doi.org/10.1063/1.1736675

Islam, U. S., Rahman, H., Abbasi, S. W., Noreen, U., & Khan., A. (2014). Suppression of fluid force on flow past a square cylinder with a detached flat plate at low Reynolds number for various spacing ratio. *Journal of Mechanical Science and Technology*, *28* (12), 4969-4978. https://doi.org/10.1007/s12206-014-1118-y

Jiang, H., & Cheng, L. (2020). Flow separation around a square cylinder at low to moderate Reynolds numbers. *Physics of Fluids*, *32*(4), 044103. https://doi.org/10.1063/5.0005757

Klotz, L., Durand, G. S., Rokicki, J., & Wesfreid, E. J. (2014). Experimental investigation of flow behind a cube for moderate Reynolds numbers. *Journal of Fluid Mechanics*, *750*, 73-98. https://doi.org/10.1017/jfm.2014.236

Krajnović, S. (2011). Flow around a tall finite cylinder explored by large eddy simulation. *Journal of fluid Mechanics*, *676*, 294-317. https://doi.org/10.1017/S0022112011000450

Kravchenko, G. A., & Moin, P. (2000). Numerical studies of flow over a circular cylinder at $Re_D = 3900$. *Physics of Fluids*, *12*(2), 403-417. https://doi.org/10.1063/1.870318

Kumar, P., & Singh, S. K. (2019). Flow past a bluff body subjected to lower subcritical Reynolds number. *Journal of Ocean Engineering and Science*, *5*(2), 173-179. https://doi.org/10.1016/j.joes.2019.10.002

Launay, G., Mignot, E., & Rivière, N. (2019). Laminar free-surface flow around emerging obstacles: Role of the obstacle elongation on the horseshoe vortex. *European Journal of Mechanics - B/Fluids*, *77*, 71–78. https://doi.org/10.1016/j.euromechflu.2019.04.006

Li, J., Chambarel, A., Donneaud, M., & Martin, R. (1991). Numerical study of laminar flow past one and two circular cylinders, *Computers & Fluids*, *19*(02), 155–170. https://doi.org/10.1016/0045-7930(91)90031-C

Liakos, A., & Malamataris, A. N. (2014). Direct numerical simulation of steady state, three dimensional, laminar flow around a wall mounted cube. *Physics of Fluids*, *26*(5), 053603. https://doi.org/10.1063/1.4876176

Lu, J. T., Stone, A. H., & Ashby, F. M. (1998). Heat transfer in open-cell metal foams. *Acta Materiala*, *46*(10), 3619-3635. https://doi.org/10.1016/S1359-6454(98)00031-7

Ma, Y., Rashidi, M. M., & Yang, Z. (2019). Numerical simulation of flow past a square cylinder with a circular bar upstream and a splitter plate downstream. *Journal of Hydrodynamics*, *31*(5), 949-964. https://doi.org/10.1007/s42241-018-0087-5

Madani, B., Topin, F., Tadrist, T., & Rigollet, F. (2007). Flow laws in metallic foams: Experimental determination of inertial and viscous contributions. *Journal of Porous Media*, *10*(1), 51-70. https://doi.org/ 10.1615/JPorMedia.v10.i1.40

Mishra, K. S., Sen, S., & Verma, A. (2021). Steady flow past a circular cylinder under large blockage. *European Journal of Mechanics - B/Fluids*, *87*, 135–150. https://doi.org/10.1016/j.euromechflu.2021.01.014

Palau-Salvador, G., Stoesser, T., & Rodi, W. (2008). LES of the flow around two cylinders in tandem. *Journal of Fluids and Structures*, *24*(8), 1304–1312. https://doi.org/10.1016/j.jfluidstructs.2008.07.002

Paterson, A. D., & Apelt, J. C. (1990). Simulation of flow past a cube in a turbulent boundary layer. *Journal of Wind Engineering and Industrial Aerodynamics*, *35*, 149-176. https://doi.org/10.1016/0167-6105(90)90214-W

Richards, J. P., Hoxey, P. R., & Short, J. L. (2001). Wind pressures on a 6m cube. *Journal of Wind Engineering and Industrial Aerodynamics*, *89*(14-15), 1553–1564. https://doi.org/10.1016/S0167-6105(01)00139-8

Saha, K. A. (2004). Three-dimensional numerical simulations of the transition of flow past a cube. *Physics of Fluids*, *16*(5), 1630–1646. https://doi.org/10.1063/1.1688324

Shang, J., Zhou, Q., Alam, M. Md., Liao, H., & Cao, S. (2019). Numerical studies of the flow structure and aerodynamic forces on two tandem square cylinders with different chamfered-corner ratios. *Physics of Fluids*, *31*(7), 075102. https://doi.org/10.1063/1.5100266

Sumner, D., Rostamy, N., Bergstrom, D. J., & Bugg, J. D. (2017). Influence of aspect ratio onthe mean flow field of a surface-mounted finite-height square prism. *International Journal of Heat and Fluid Flow*, *65*, 1–20. https://doi.org/10.1016/j.ijheatfluidflow.2017.02.004

Visbal, R. M. (1991). Structure of laminar juncture flows. *AIAA Journal*, *29*(8), 1273-1282. https://doi.org/10.2514/3.10732

Zhang, D., Cheng, L., An, H., & Zhao, M. (2017). Direct numerical simulation of flow around a surface mounted finite square cylinder at low Reynolds numbers. *Physics of Fluids*, *29*(4), 045101. https://doi.org/10.1063/1.4979479

Zhang, X. F., Yang, J. C., Ni, M. J., Zhang, N. M., & Yu, X. G. (2022). Experimental and numerical studies on the three-dimensional flow around single and two tandem circular cylinders in a duct. *Physics of Fluids*, *34* (03), 033610. https://doi.org/10.1063/5.0084764.

Zhao, M., Al Mamoon, A., & Wu, H. (2021). Numerical study of the flow past two wall-mounted finite-length square cylinders in tandem arrangement. *Physics of Fluids*, *33*(9), 093603. https://doi.org/10.1063/5.0058394

Zhou, Q., Alam, M. Md., Cao, S., Liao, H., & Li, M. (2019). Numerical study of wake and aerodynamic forces on two tandem circular cylinders at Re = 10^3. *Physics of Fluids*, *31*(4), 045103. https://doi.org/10.1063/1.5087221